

Deconvolution of multi-Boltzmann x-ray distribution from linear absorption spectrometer via analytical parameter reduction

Cite as: *Rev. Sci. Instrum.* **92**, 113102 (2021); doi: [10.1063/5.0057486](https://doi.org/10.1063/5.0057486)

Submitted: 21 May 2021 • Accepted: 18 October 2021 •

Published Online: 5 November 2021



View Online



Export Citation



CrossMark

C. D. Armstrong,^{1,a)}  D. Neely,^{1,b)}  D. Kumar,²  P. McKenna,³  R. J. Gray,³  and A. S. Pirozhkov^{4,a)} 

AFFILIATIONS

¹Central Laser Facility, Rutherford Appleton Laboratory, Harwell OX110QX, United Kingdom

²Department of Radiation and Chemical Physics, Institute of Physics of the Czech Academy of Sciences, Na Slovance 1999/2, 18221 Prague 8, Czechia

³SUPA Department of Physics, University of Strathclyde, Glasgow G4 0NG, United Kingdom

⁴Kansai Photon Science Institute, National Institutes for Quantum and Radiological Science and Technology, 8-1-7 Umemidai, Kizugawa, Kyoto 619-0215, Japan

^{a)}Authors to whom correspondence should be addressed: chris.armstrong@stfc.ac.uk and pirozhkov.alexander@qst.go.jp

^{b)}Deceased.

ABSTRACT

Accurate characterization of incident radiation is a fundamental challenge for diagnostic design. Herein, we present an efficient spectral analysis routine that is able to characterize multiple components within the spectral emission by analytically reducing the number of parameters. The technique is presented alongside the design of a hard x-ray linear absorption spectrometer using the example of multiple Boltzmann-like spectral distributions; however, it is generally applicable to all absorption based spectrometer designs and can be adapted to any incident spectral shape. This routine is demonstrated to be tolerable to experimental noise and suitable for real-time data processing at multi-Hz repetition rates.

© 2021 Author(s). All article content, except where otherwise noted, is licensed under a Creative Commons Attribution (CC BY) license (<http://creativecommons.org/licenses/by/4.0/>). <https://doi.org/10.1063/5.0057486>

I. INTRODUCTION

Hard x-ray emission from high intensity laser interactions with solid targets is a broad spectral distribution extending up to the peak energies of the accelerated electrons. Careful characterization of this emission can inform us about the properties of the population of energetic electrons propagating within the target, rather than measuring it after escaping the sheath potential, which is known to reduce the measured electron energies.¹ Numerous diagnostic techniques have been demonstrated^{2–5} with several early methods relying on an image plate and metallic filters in both linear⁴ and areal layouts.⁵ Rusby *et al.* presented an active method that relied upon scintillator crystals to both attenuate and detect the incident radiation.² The design used here is an adaptation to this technique, presented initially by Armstrong,⁶ that utilizes tungsten filters and Lu_{1.8}Y_{0.2}SiO₅ (LYSO) scintillators to make a more compact rail that can operate both inside and outside a vacuum chamber—filtering

from the external flange must be considered in the latter case. These types of designs are a key method of characterizing x-ray energies between the limit of *k*-edges (~100 keV) and the onset of activation (~8 MeV), and therefore, accurate reconstruction is a pertinent area of study.

Each of these designs has involved a spectral reconstruction approach that followed a similar routine. First, the diagnostic and filters are simulated using Monte Carlo codes to build a response matrix. Then, using a predefined spectral shape, trial responses can be generated and compared to the measured data. These spectral shapes can often be expressed as dependent on two variables: flux and a control (temperature, critical energy, bandwidth, etc.). This trial process relies on both an adequate fitting routine that can handle a wide dynamic range and the incident radiation to be approximated by a distribution with a single control parameter, such as temperature. In such a case, it is possible to simply scan the desired parameter space varying the flux and control

variable of the trial spectra to find the closest match to the data. However, if the incident spectral distribution is more complex, with multiple components, this process quickly becomes intractable.

The emission from solid targets is expected to broadly follow the accelerated electron population and exhibit a Boltzmann-like distribution with multiple temperature components.^{4,7-9} Emissions from laser-wakefield interactions typically have both a bremsstrahlung-like distribution and the characteristic betatron spectra,¹⁰ the former seeded from electrons interacting with any shielding or filtering in the beam. In each case, for two-component distributions, characterizing the emission requires scanning through four independent parameters: the flux and temperature/critical energy of the first component and the flux and temperature/critical energy of the second. One can envision more complicated incident spectral shapes that contain additional components within the emission, each requiring a flux and control parameter to be deconvolved. This is generally how solutions to single temperature approximations are found;^{2-4,9} however, scaling this method to multiple temperature components is inefficient as one needs to calculate a large $2 \times N$ dimensional parameter space to find the best match to the measured data. Chen *et al.*^{4,9} discussed the application of a two-temperature fitting routine when outlining the diagnostic response, utilizing a normalized ratio, R_{Chen} , of two temperatures between 10 keV and 10 MeV of the form

$$f(E) \propto R_{Chen} \exp(-E/T_{cold}) + \exp(-E/T_{hot}), \quad (1)$$

where T_{cold} and T_{hot} are the temperatures of each distribution. This method aims to short cut the problem of four dimensional space by first normalizing the emission and then scanning over the three parameters; however, the total flux would still need to be calculated after the fact as the fourth parameter, which still leaves this as a 4D problem.

In this paper, we present a novel approach that reduces the number of explicit variables that need to be scanned by directly calculating the optimum flux for each spectral component, i.e., the number of photons, n_i , that minimizes the difference between the measured data and the trial spectra for a given set of control variables. Applying this technique to the measurement of the multiple components of an x-ray distribution can provide insight into the underlying physical processes, such as isolating a low-energy thermal emission that can otherwise dominate the interaction⁶ or probing an energetic but low flux component of the emission.^{4,9} This opens up the potential to investigate new physical processes as lasers approach the QED regime,^{11,12} where strong-field processes can manifest as energetic peaks in the photon emission^{11,13}—distinct in spectral distribution yet emanating from the same laser–plasma interaction as bremsstrahlung emission from classical collisional processes. We note that depending on the interaction details, such as the presence of preplasma and electron distribution function, the QED regimes can produce Boltzmann-like distributions as well, as in the following simulations exhibiting no signs of decreased spectral density at low photon energies.¹⁴⁻¹⁷ Thus, the ability to deal with multi-component Boltzmann-like distributions and to distinguish them from non-Boltzmann distributions is of major interest for the present and future experiments.

II. LINEAR ABSORPTION SPECTROMETER DESIGN

The first step in reconstructing the incident spectra is creating a response matrix, Γ , for the given spectrometer design. This can be calculated using Monte Carlo simulations, such as GEANT4,¹⁸ to determine the energy deposited in each layer of the spectrometer as a function of photon energy. This technique can be generally applied to any form of attenuation based spectrometer; however, the results presented below are based on the design initially presented in Ref. 6. This design consists of ten $2 \times 10 \times 30$ mm³ LYSO ($\text{Lu}_{1.8}\text{Y}_{0.2}\text{SiO}_5$) scintillator crystals positioned in a linear array with five tungsten filters of the same dimensions interspersed in the latter half of the spectrometer, with a total length, L , of the spectrometer to be ~ 60 mm. The crystals and filters are held in a 3D printed frame that optically isolates the front crystals and aligns the output plane to the collection lens. The lens in question should be as fast (high NA) as possible to ensure high collection efficiency of the emitted light, and the scintillators should be wrapped in a high-reflectivity coating^{19,20} to maximize the fraction of emitted optical light. These factors and the inherent conversion efficiency of the scintillator should then be considered to absolutely calibrate the device, i.e., determine the conversion between detected light (counts) and absorbed energy in each crystal.²⁰

The scintillators are then positioned within a lead housing that acts both as a partial collimator and as a protection from scattered radiation. However, as the x rays are geometrically expanding over the source to spectrometer distance, Z , there is a relative fluence change between the first and last crystal that should be accounted for in the generation of the response matrix. This effect can be considered negligible provided $Z \gg L$. Γ should, also, include the absolute conversion between the energy deposited and light detected on the CCD to permit a direct comparison between measured and expected data. The generation of the response matrix should include the specifics for each experimental setup, for example, if the device is situated inside the vacuum chamber, one only needs to account for any attenuation due to light tightening, but if it is outside, the flange should be accounted for.

A schematic of the diagnostic is shown in Fig. 1(a), and typical experimental setups and photos can be found in Refs. 2 and 6. When used in laser–plasma interactions, the diagnostic is also used together with a permanent magnetic field to remove charged particles from the incident radiation. This specific design has been used already in several studies;^{6,21} LYSO was selected due to its high density, effective Z , and relative light output in comparison to other scintillator materials.

In the response matrix shown in Fig. 2, there is attenuation at lower energies due to a 12 mm Al flange. If there are further materials in the way, the response matrix should be recalculated to address these specifics, and more broadly, when altering the layout of the scintillator crystals within the spectrometer, a new response matrix is required. However, the reconstruction technique described herein is generally applicable, regardless of the specific filter/scintillator layout.

Of note in the response shown is how the latter scintillator responses begin to exceed the first crystal response as the incident energy increases and the discontinuity at ~ 60 keV. The former is due to secondary x rays (predominantly 511 keV, generated through electron–positron annihilation) being generated in the first crystal

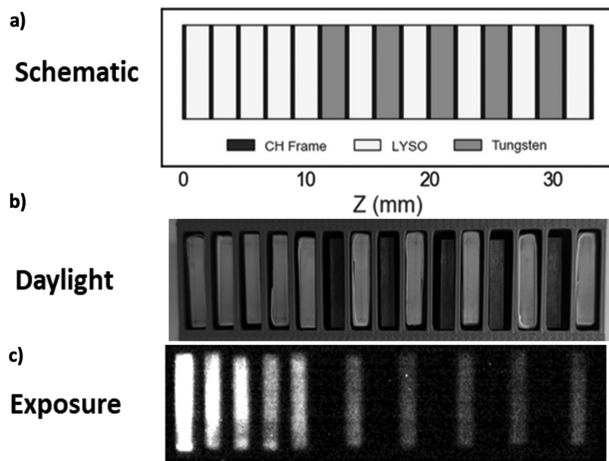


FIG. 1. HxLAS scintillator design. (a) The schematic of the design with LYSO and tungsten elements labeled, (b) a photograph of the diagnostic, and (c) an example exposure to x-ray radiation taken as part of the experimental study in Ref. 21.

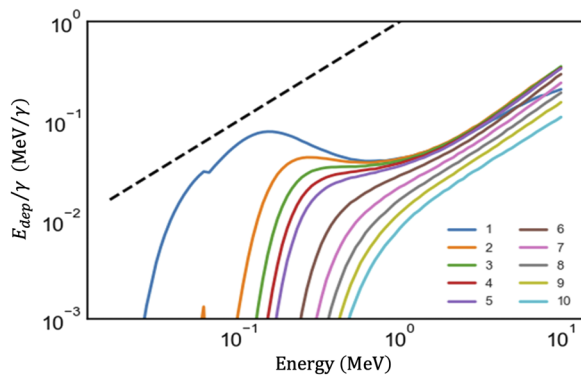


FIG. 2. Response curves as a function of energy for each crystal in the HxLAS determined via Monte Carlo simulations of single energy photons. The incident photon energy is shown in MeV, and the energy deposited is shown in MeV/gamma. The dashed line corresponds to the full absorption of the photon energy.

and propagating through the array. However, the latter is due to the Lu k -edge in LYSO.

III. ANALYSIS ROUTINE

A. Analytical derivation

With the response matrix for single energies determined, we are able to calculate how the spectrometer will respond to an incident spectral distribution. The emission from solid targets is expected to broadly follow the accelerated electron population and exhibit a Boltzmann-like distribution with multiple temperature components.^{7,8} This is seen in both simulations²² and experimental measurements alike^{4,9} and arises due to a myriad of complex and competing processes—for example, multiple absorption mechanisms to couple energy to the electron population^{22,23} or variations

in electron energy due to interactions with the sheath field.¹ However, the approach can be generalized to any incident spectral shape, and so we define

$$F(E_\gamma) = \sum_{i=1}^N n_i f_i(E_\gamma, T_i), \quad (2)$$

where F is the total spectral distribution as a function of photon energy, E_γ . $F(E_\gamma)$ represents the summation of multiple spectral components, f_i , each of which is, in turn, dependent on photon energy, the flux of each component, n_i , and a control parameter, T_i , for the given spectral shape. The control parameters vary depending on the spectral shape; however, for Boltzmann-like spectra, this would be temperature, and for synchrotron-like spectra, this would be critical energy. f_i has i as a subscript to outline that it is possible to consider multiple spectral shapes as well as components—i.e., a peak with a thermal distribution. With this defined, we can outline that our measured data are therefore the product of this spectral shape and our response matrix, Γ , integrated over all energies. The response matrix and, therefore, the measured signals, M_k , are a function of the crystal number, k ,

$$M_k = \int_0^\infty F(E_\gamma) \Gamma(k, E_\gamma) dE_\gamma. \quad (3)$$

In order to solve for $F(E_\gamma)$, we can use a trial solution S_k that is the summation of a set number of spectral components with parameters n_1, T_1, n_2, T_2 , etc.,

$$S_k = n_1 \int_0^\infty f_1(E_\gamma, T_1) \Gamma(k, E_\gamma) dE_\gamma + n_2 \int_0^\infty f_2(E_\gamma, T_2) \Gamma(k, E_\gamma) dE_\gamma + \dots, \quad (4)$$

where f_i is the desired spectral shapes to be used—this can be extended as necessary, and the equation can be rewritten as

$$S_k = \sum_{i=1}^N n_i r_{ik}, \quad (5)$$

where r_{ik} is the single photon response for each crystal, k , and each spectral component, i ,

$$r_{ik} = \int_0^\infty f_i(E_\gamma, T_i) \Gamma(k, E_\gamma) dE_\gamma. \quad (6)$$

This expression for the reduced response can be pre-calculated for each form of f_i , as it is independent of the measured data. We wish to find the best fit between our trial spectra and the measured data in order to determine the parameters in F , and so we can look to minimize the difference between the measured signal and the trial solution through a sum of squares expression

$$\phi = \sum_{k=1}^K \left(\frac{M_k - S_k}{X_k} \right)^2, \quad (7)$$

where X_k is a normalization that we can apply as necessary—either the measured value (M_k) itself or the standard error/uncertainty (δM_k) associated with each crystal. In cases where the uncertainty is high, e.g., low count levels across crystals, using δM_k can help mitigate over-fitting in the routine. Here, K is the total number of

scintillators in the spectrometer (ten in our case). From the merit function, ϕ , and the expression for S_k previously defined, we can re-express as a function of the normalized data, Q_k , and reduced response, $R_{i,k}$,

$$Q_k = \frac{M_k}{X_k}, R_{i,k} = \frac{r_{i,k}}{X_k}, \quad (8)$$

$$\begin{aligned} \phi &= \sum_{k=1}^K \left(Q_k - \sum_{i=1}^N n_i R_{i,k} \right)^2 \\ &= \left(\mathbf{Q} - \sum_{i=1}^N n_i \cdot \mathbf{R}_i \right)^2. \end{aligned} \quad (9)$$

Here, we use a standard notation where the central dot denotes a dot product. We can directly solve for the minimum of this merit function by computing the derivatives $\partial\phi/\partial n_i$ and equating them to zero. We note that Eq. (9) is a quadratic form with ϕ tending to $+\infty$ when any of n_i tends to $\pm\infty$, i.e., the only zero-derivative point, $n(T_i) = [n_1, n_2, \dots]$, is the solution corresponding to single ϕ 's minimum for the given temperatures, T_i . This leaves us with a system of N linear equations with N variables as follows:

$$n_i \cdot \mathbf{R}_i \cdot \mathbf{R}_i^T = \mathbf{Q} \cdot \mathbf{R}_i^T, \quad (10)$$

where \mathbf{R}_i^T denotes a transposed matrix. This equation system is easily solvable by any of the available methods—we used the *Solve* function in the Mathematica software.²⁴ We provide explicit solutions for one-, two-, and three-temperature cases in the Appendix.

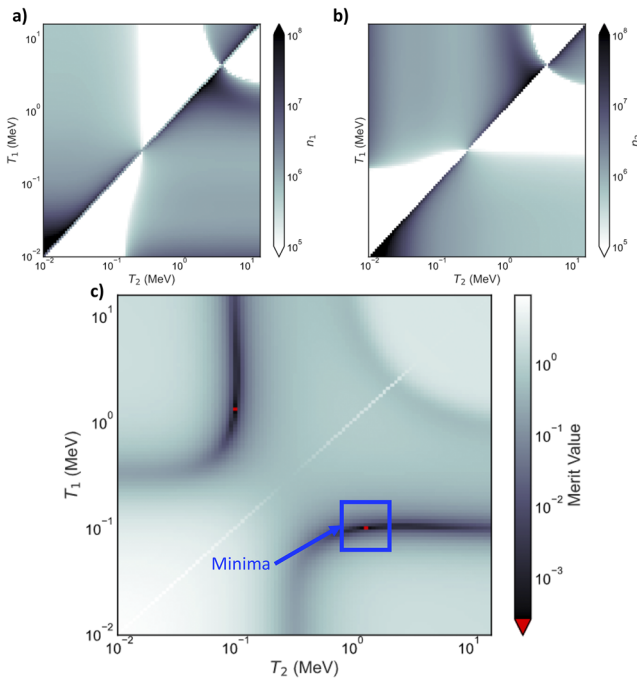


FIG. 3. Example of reconstruction via the analytically reduced method. (a) and (b) are the sparse grids for the number of photons in each spectral component, n_1 (a) and n_2 (b) for the temperature range between 0.1 and 25 MeV. (c) shows the merit function ϕ for the same temperature range—the two red points indicate the minimum values and therefore best fit.

TABLE I. Input flux and temperature parameters for the example response used in the deconvolution.

| Input parameters | | | |
|------------------|-----|---------|-----------------|
| | i | 1 | 2 |
| Flux | n | 10^6 | 5×10^5 |
| Temperature | T | 100 keV | 1.4 MeV |

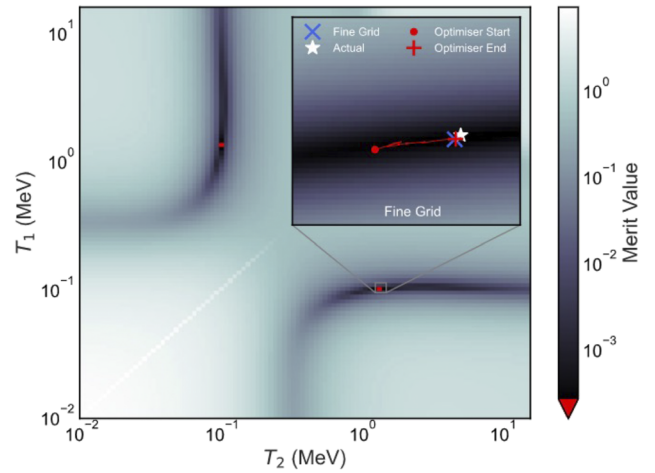


FIG. 4. Example of second stage reconstruction. From the sparse grid shown in Fig. 3(c), we can either compute a fine grid around the minima or use a Nelder–Mead routine about the same space. The inset shows the parameter space evaluated by the fine grid, and the red line shows the evaluation points for the NM routine—the color scale of the inset is the same as the primary figure.

For some sets of temperatures, some of the n_i values can be negative, which is clearly unphysical and, as such, we set them to be zeros. This does not represent a problem as it can only happen away from the sought-for optimum solution.

B. Example case

The routine, and an example of the negative values in calculating n_1, n_2 , is demonstrated in Fig. 3 for two Boltzmann-like distributions with the parameters given in Table I.

First, the expected values are generated from the response matrix and a random noise is added, i.e., a random factor in the interval $[-2\%, +2\%]$ is applied to the data. Second, a sparse grid of temperatures is constructed of 100 logarithmically spaced steps

TABLE II. Initial flux and temperature parameters for the unguided optimization routine; the square brackets here express a range over which the values are randomly selected.

| Unguided routine | | | |
|------------------|-----|-----------------|-----------------|
| | i | 1 | 2 |
| Flux | n | $[10^1, 10^8]$ | $[10^1, 10^8]$ |
| Temperature | T | $[0.1, 10]$ MeV | $[0.1, 10]$ MeV |

TABLE III. Initial flux and temperature parameters for the “best guess” optimization routine; the temperature is fixed in line with expected values from a high intensity laser interaction and the flux taken from the first and fifth crystal values.

| Best guess routine | | | |
|--------------------|-----|---------|-------|
| | i | 1 | 2 |
| Flux | n | M_1 | M_5 |
| Temperature | T | 0.1 MeV | 1 MeV |

between 0.1 and 25 MeV. For each set of temperatures, n_1 and n_2 are determined via solutions to Eq. (10) (shown explicitly in the Appendix) and the expected parameters used to compute the merit function ϕ . In this example, we take $X_k = M_k$ and therefore set $Q_k = 1$. The white spaces in Figs. 3(a) and 3(b) are regions where the solution for n_1 or n_2 was negative, and due to the symmetry of the parameter space, (b) is the transpose of (a). The diagonal lines with significantly different values of n_1 , n_2 , and ϕ on panels (a), (b), and (c), respectively, in Fig. 3 correspond to the optimal value of n_1 for the case of a single spectral component, as described by Eq. (A1) in the Appendix.

The two symmetric minima of this sparse array are close approximations to the correct answer, and these two fits

represent the same solution with swapped T_1 and T_2 . At this point, we can either refine the test grid with smaller intervals over a narrow range about these minima or use local minimization routines such as Nelder–Mead or Powell.^{25,26} The sparse grid guarantees that we are close to the global minima of the parameter space and either final step is able to finalize the optimization. The inset of Fig. 4 compares the respective performance of these methods toward converging to the optimal solution.

C. Comparison to other methods

Minimization or optimization routines, such as Nelder–Mead or Powell,^{25,26} are an active area of study. These techniques, in general, seek to find efficient ways to explore multi-dimensional parameter spaces and find the best comparison based on some criteria (or merit function) starting from a defined or random position within a said parameter space. We now compare the result from the Nelder–Mead to a variety of start positions, “unguided,” “best-guess,” and the output from the first stage of this routine, to the fine grid calculation. The starting parameters for these routines are expressed in Tables II and III; unguided uses a random start position over the expected space—with the larger of the two fluxes corresponding to the lower of the two temperatures to fit the typical values we expect. The “best-guess” routine uses the measured

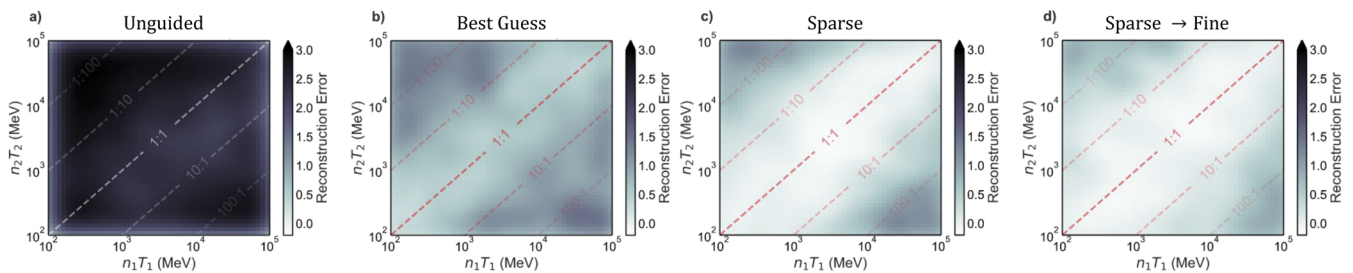


FIG. 5. Comparison of methods of second stage reconstruction; the color/gray scale is the reconstruction error [Eq. (11)]. Panels (a)–(c) set the start position for a Nelder–Mead optimizer as “unguided,” “best-guess,” and the output from the first stage of this routine, respectively. Panel (d) uses a fine grid as the second stage reconstruction. Contours of energy ratios are shown as dashed lines with the ratio expressed as $n_1 T_1 / n_2 T_2$.

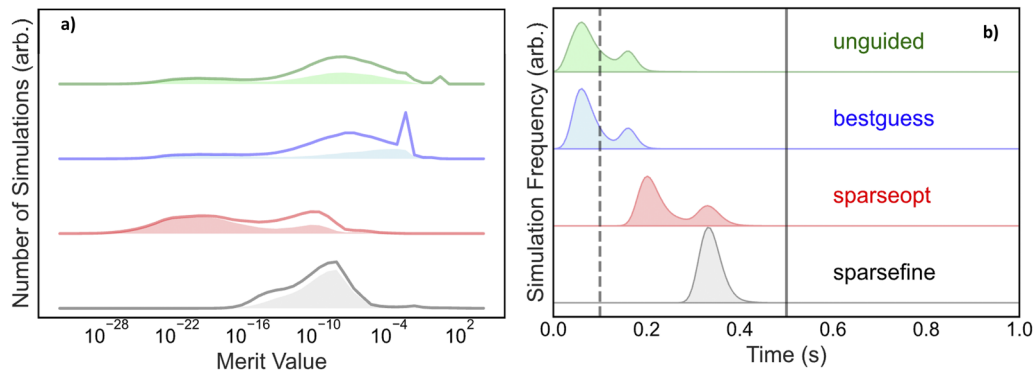


FIG. 6. (a) Comparison of the merit value (figure of merit between simulated and reconstructed *data*) to reconstruction error (figure of merit between input and reconstructed *spectral parameters*)—solid line indicates the number of reconstructions at each merit value, and the filled region is the number of those that have a reconstruction error < 2 . (b) Averaged computation time for each methodology on a standard desktop machine. The vertical solid and dashed lines correspond to 2 and 10 Hz reconstructions, respectively.

crystal values of the first and fifth crystals as the initial flux and 0.1 and 1 MeV temperature for T_1 and T_2 , respectively. These initial values are chosen to approximate the typical emission seen from other similar diagnostics^{2,4,9} and could be altered to suit different laser parameters.

In both cases, we find that the solutions are typically poorer than either of the sparse grid methods. Figure 5 demonstrates the reliability of reconstruction for each method. To generate this graph, we computed 10 000 input spectra with n_1 , n_2 between 10 and 10^6 and T_1 , T_2 between 0.1 and 10 MeV. To measure the success

of the reconstruction, we can take the mean error of the reconstructed parameters divided by the input and record this value for each simulation. Namely, the reconstruction error is calculated as follows:

$$\frac{1}{4} \left(\frac{|T_1^* - T_1|}{T_1} + \frac{|n_1^* - n_1|}{n_1} + \frac{|T_2^* - T_2|}{T_2} + \frac{|n_2^* - n_2|}{n_2} \right), \quad (11)$$

where the stars denote the reconstructed values.

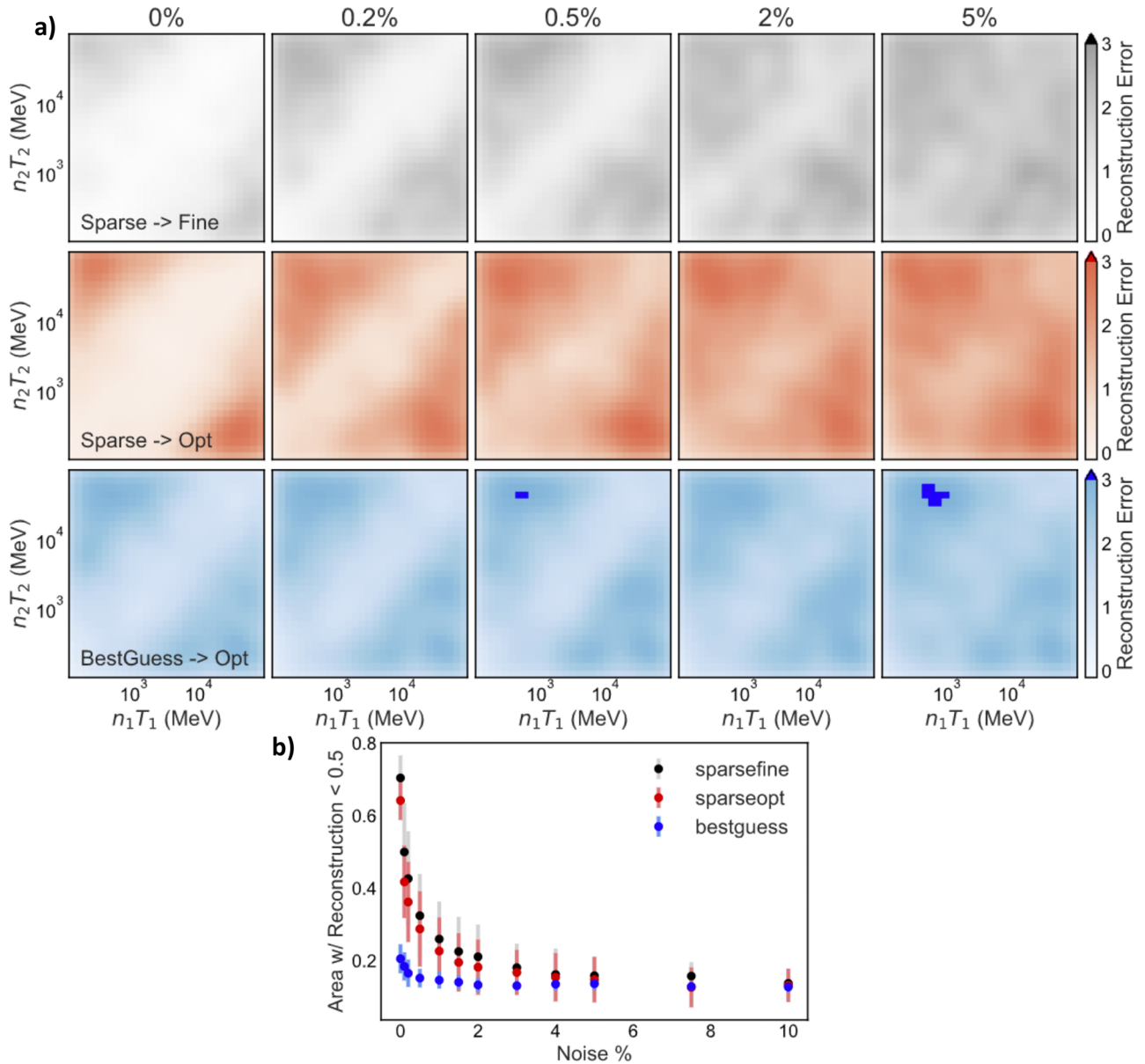


FIG. 7. Comparison for routines “sparsefine”—black, “sparseopt”—red, and “bestguess”—blue, showing the reconstruction values with increasing levels of noise. (a) shows the parameter space for each routine, and (b) shows the area over the parameter space that the routines are able to achieve good reconstruction.

In Fig. 5, this is plotted as a function of the effective energy in each spectral component calculated as $n_1 T_1$ and $n_2 T_2$. By doing this, we see the region over which the different methods are able to accurately reconstruct the input parameters. For each method using the sparse routine, we are able to reliably reconstruct over a significantly larger proportion of the parameter space than either the “unguided” or “best guess.”

IV. DISCUSSION

While Fig. 5 demonstrates a poor reconstruction for both the unguided routines, each technique can typically find a good merit value. This demonstrates a concern relating to these diagnostics in general. Each routine typically produces a *precise* match between the data and the trial data (low merit value); however, the *accuracy* of the reconstructed parameters [Eq. (11)] is poorer for both the “unguided” or “best guess” routines. This highlights that there can be an element of non-unicity to solutions. Figure 6(a) outlines that this effect is exacerbated in the purely optimizer routines, the top two curves. Figures 5 and 6(a) show that incorrect reconstructions are less frequent for the analytical approaches presented in this manuscript and only occur when one of the two temperature components has a negligible energy (nT) compared with another. To reiterate this point, we see in Fig. 6(a) that a merit value of 10^{-10} is readily achieved by all techniques, yet only the sparse-fine routine demonstrates good accuracy in the reconstructed values. While not explored in this article, there is scope for improved designs of spectrometers that minimize the non-unicity of solutions.

Diagnostics like these are well suited to existing ~ 0.1 Hz facilities^{27–30} as well as upcoming high repetition laser facilities³¹ due to the high repetition nature of the scintillators and cameras. As such, it is important to have analysis routines that can find a solution faster than the laser repetition rate, and from the results in Fig. 6(b), we see that this routine—on a standard desktop machine—would suit for systems operating up to a few Hz, with scope for improvement, either through more efficient code development or faster machines.

In experimental situations, this analysis routine will need to address noise in the data—from each crystal, we can get a measure of the uncertainty through the standard deviation across the crystal and set that as X_k in Eq. (9). This measure should factor into the layout and geometry of the spectrometer in the experiment, as one should seek to maximize the signal-to-noise ratio (SNR) by positioning the spectrometer as close to target as possible. Recent measurements with the linear absorption spectrometer design reported herein have demonstrated typical noise values between 0.3% and 2.5%.³²

Figure 7 shows the result from adding 0% to 10% Gaussian noise prior to reconstruction, and we see that for the routines, the area of accurate reconstruction decreases significantly with increasing noise levels. The merit function with X_k set to the error of each crystal value can be used to find the deviation of the experimental spectra from the expected model. For example, if the model used was a several-temperature Boltzmann distribution, the reconstruction resulted in large merit function values that would be a strong indication of non-Boltzmann component presence. Certainly, this method is more sensitive when the experimental error bars are small,

which is a simple consequence of the fact that a non-Boltzmann component should not be buried within the experimental noise.

This technique can be generalized beyond the summation of thermal distributions since Eq. (3) is independent of spectral shape. Defining several response types for r_i —for example, a thermal distribution and a peaked distribution—would allow the routine to probe for hidden features without necessitating a significant change in the algorithm. Each spectral shape would need to be defined by a single flux and control parameter, such as critical energy for synchrotron emission.

V. SUMMARY

In summary, we present a novel solution to determining complex spectral distributions from attenuation based diagnostics. This works by first reducing the number of explicit variables by half (e.g., 4D to 2D for a two-temperature distribution). The routine, in short, follows this operation:

- (i) Simulate the spectrometer response to individual photon energies.
- (ii) Calculate the spectrometer response to single-photon distributions in expected spectral component shape.
- (iii) Scan a low-resolution (sparse) parameter space, solving for optimum flux for each set of control parameters.
- (iv) At optimum, defined by a merit function [Eq. (9)], rescan through a high-resolution grid or optimizer routine.

We present a comparison of this routine with unguided techniques, demonstrating the significant increase in accuracy over a wider region of input conditions for the technique presented here. We outline the tolerance to experimental noise and uncertainty and demonstrate that the computation time for this technique—while longer than reconstructions via either a blind technique—is suitable for online operation for upcoming Hz-level repetition rate high power laser facilities on a standard desktop. With accurate measurement and deconvolution of these higher order terms within emitted x-ray spectra, we can better understand the internal plasma processes occurring. This technique can be applied to numerous spectral functions/shapes—by altering the response r_i in Eqs. (3) and (9) to that of a synchrotron-like emission or inverse-Compton spectra or a combination of thermal and non-thermal components—which greatly increases what we can reliably reconstruct with absorption based x-ray spectrometers.

SUPPLEMENTARY MATERIAL

See the [supplementary material](#) for the derivation of solutions to the system of linear equations [Eq. (10)] for the case where $N = 1, 2, 3$.

ACKNOWLEDGMENTS

We acknowledge the support of the experimental staff at both the Central Laser Facility and Kansai Photon Science Institute through which experimental experience with the diagnostic was possible. This work was funded by the QST-IRI, the QST President’s Strategic Grant (Creative Research) No. 20, the JSPS KAKENHI (Grant No. JP19H00669), and the EPSRC (Grant No.

EP/R006202/1). This research was also supported by the Czech Science Foundation (Project No. 18-09560S).

Professor David Neely sadly passed away before this work was published; he was a colleague, mentor, and friend to the authors.

AUTHOR DECLARATIONS

Conflict of Interest

The authors have no conflicts to disclose.

DATA AVAILABILITY

The input data and necessary code samples that support the findings of this study are openly available at <http://dx.doi.org/10.5286/edata/748>.

APPENDIX: SOLUTIONS TO SYSTEM OF LINEAR EQUATIONS

The equations below are the solutions to the system of linear equations [Eq. (10)] for the case where $N = 1, 2, 3$. Within

these expressions, the terms R_{ij} refer to the dot product of R_i and R_j —the reduced response in Eq. (6) of the i th and j th components, respectively—and QR_i denotes the dot product of Q and R_i —when X_k in the merit function is M_k , this reduces to simply the sum of R_i . Throughout, Q and R_i are vectors of length K .

The derivations for each of these equations are shown in the [supplementary material](#) for both cases where X_k in the merit function is M_k and Q reduces to 1 and, alternatively, where X_k is set to the uncertainty in the data and Q does not reduce so simply. This method can also be extended to increasing numbers of components by solving Eq. (10) for more terms.

For a single temperature distribution,

$$n_1 = \frac{QR_1}{R_{11}}. \quad (\text{A1})$$

For two temperatures,

$$\begin{aligned} n_1 &= \frac{QR_2R_{12} - QR_1R_{22}}{R_{12}^2 - R_{11}R_{22}}, \\ n_2 &= \frac{-QR_2R_{11} + QR_1R_{12}}{R_{12}^2 - R_{11}R_{22}}. \end{aligned} \quad (\text{A2})$$

For three temperatures,

$$\begin{aligned} n_1 &= \frac{QR_3R_{13}R_{22} - QR_3R_{12}R_{23} - QR_2R_{13}R_{23} + QR_1R_{23}^2 + QR_2R_{12}R_{33} - QR_1R_{22}R_{33}}{R_{13}^2R_{22} - 2R_{12}R_{13}R_{23} + R_{11}R_{23}^2 + R_{12}^2R_{33} - R_{11}R_{22}R_{33}}, \\ n_2 &= \frac{-QR_3R_{12}R_{13} + QR_2R_{13}^2 + QR_3R_{11}R_{23} - QR_1R_{13}R_{23} - QR_2R_{11}R_{33} + QR_1R_{12}R_{33}}{R_{13}^2R_{22} - 2R_{12}R_{13}R_{23} + R_{11}R_{23}^2 + R_{12}^2R_{33} - R_{11}R_{22}R_{33}}, \\ n_3 &= \frac{QR_3R_{12}^2 - QR_2R_{12}R_{13} - QR_3R_{11}R_{22} + QR_1R_{13}R_{22} + QR_2R_{11}R_{23} - QR_1R_{12}R_{23}}{R_{13}^2R_{22} - 2R_{12}R_{13}R_{23} + R_{11}R_{23}^2 + R_{12}^2R_{33} - R_{11}R_{22}R_{33}}. \end{aligned} \quad (\text{A3})$$

REFERENCES

- ¹D. R. Rusby, C. D. Armstrong, G. G. Scott, M. King, P. McKenna, and D. Neely, "Effect of rear surface fields on hot, refluxing and escaping electron populations via numerical simulations," *High Power Laser Sci. Eng.* **7**, E45 (2019).
- ²D. R. Rusby, C. D. Armstrong, C. M. Brenner, R. J. Clarke, P. McKenna, and D. Neely, "Novel scintillator-based x-ray spectrometer for use on high repetition laser plasma interaction experiments," *Rev. Sci. Instrum.* **89**, 073502 (2018).
- ³K. T. Behm, J. M. Cole, A. S. Joglekar, E. Gerstmayr, J. C. Wood, C. D. Baird, T. G. Blackburn, M. Duff, C. Harvey, A. Ilderton *et al.*, "A spectrometer for ultrashort gamma-ray pulses with photon energies greater than 10 MeV," *Rev. Sci. Instrum.* **89**, 113303 (2018).
- ⁴C. D. Chen, J. A. King, M. H. Key, K. U. Akli, F. N. Beg, H. Chen, R. R. Freeman, A. Link, A. J. Mackinnon, A. G. MacPhee *et al.*, "A Bremsstrahlung spectrometer using k -edge and differential filters with image plate dosimeters," *Rev. Sci. Instrum.* **79**, 10E305 (2008).
- ⁵R. H. H. Scott, E. L. Clark, F. Pérez, M. J. V. Streeter, J. R. Davies, H.-P. Schlenvoigt, J. J. Santos, S. Hulin, K. L. Lancaster, S. D. Baton *et al.*, "Measuring fast electron spectra and laser absorption in relativistic laser-solid interactions using differential bremsstrahlung photon detectors," *Rev. Sci. Instrum.* **84**, 083505 (2013).
- ⁶C. D. Armstrong, "Bremsstrahlung radiation and fast electron transport in laser-plasma interactions," Ph.D. thesis, University of Strathclyde, 2019.

- ⁷A. Compant La Fontaine, C. Courtois, and E. Lefebvre, "Production of multi-MeV bremsstrahlung x-ray sources by petawatt laser pulses on various targets," *Phys. Plasmas* **19**, 023104 (2012).
- ⁸C. Courtois, R. Edwards, A. Compant La Fontaine, C. Aedy, S. Bazzoli, J. L. Bourgade, J. Gazave, J. M. Lagrange, O. Landoas, L. L. Dain *et al.*, "Characterisation of a MeV Bremsstrahlung x-ray source produced from a high intensity laser for high areal density object radiography," *Phys. Plasmas* **20**, 083114 (2013).
- ⁹C. D. Chen, P. K. Patel, D. S. Hey, A. J. Mackinnon, M. H. Key, K. U. Akli, T. Bartal, F. N. Beg, S. Chawla, H. Chen *et al.*, "Bremsstrahlung and $K\alpha$ fluorescence measurements for inferring conversion efficiencies into fast ignition relevant hot electrons," *Phys. Plasmas* **16**, 082705 (2009).
- ¹⁰F. Albert and A. G. R. Thomas, "Applications of laser wakefield accelerator-based light sources," *Plasma Phys. Controlled Fusion* **58**, 103001 (2016).
- ¹¹C. P. Ridgers, C. S. Brady, R. Duclous, J. G. Kirk, K. Bennett, T. D. Arber, A. P. L. Robinson, and A. R. Bell, "Dense electron-positron plasmas and ultraintense γ rays from laser-irradiated solids," *Phys. Rev. Lett.* **108**, 165006 (2012).
- ¹²T. Nakamura, J. K. Koga, T. Z. Esirkepov, M. Kando, G. Korn, and S. V. Bulanov, "High-power γ -ray flash generation in ultraintense laser-plasma interactions," *Phys. Rev. Lett.* **108**, 195001 (2012).
- ¹³R. Capdessus, M. King, D. Del Sorbo, M. Duff, C. P. Ridgers, and P. McKenna, "Relativistic Doppler-boosted γ -rays in high fields," *Sci. Rep.* **8**, 9155 (2018).

- ¹⁴C. P. Ridgers, J. G. Kirk, R. Ducloux, T. G. Blackburn, C. S. Brady, K. Bennett, T. D. Arber, and A. R. Bell, "Modelling gamma-ray photon emission and pair production in high-intensity laser-matter interactions," *J. Comput. Phys.* **260**, 273–285 (2014).
- ¹⁵K. V. Lezhnin, P. V. Satorov, G. Korn, and S. V. Bulanov, "High power gamma flare generation in multi-petawatt laser interaction with tailored targets," *Phys. Plasmas* **25**, 123105 (2018).
- ¹⁶Y.-J. Gu, O. Klimo, S. V. Bulanov, and S. Weber, "Brilliant gamma-ray beam and electron-positron pair production by enhanced attosecond pulses," *Commun. Phys.* **1**, 93 (2018).
- ¹⁷J. Vysocil, "Gamma rays from solid targets irradiated by ultra-intense laser beams," Ph.D. thesis, Czech Technical University of Prague, 2019.
- ¹⁸J. Allison, K. Amako, J. Apostolakis, P. Arce, M. Asai, T. Aso, E. Bagli, A. Bagulya, S. Banerjee, G. Barrand *et al.*, "Recent developments in Geant4," *Nucl. Instrum. Methods Phys. Res., Sect. A* **835**, 186–225 (2016).
- ¹⁹J. T. M. De Haas, P. Dorenbos, and C. W. E. Van Eijk, "Measuring the absolute light yield of scintillators," *Nucl. Instrum. Methods Phys. Res., Sect. A* **537**, 97–100 (2005).
- ²⁰A. Dasgupta, C. D. Armstrong, D. Neely, D. R. Rusby, and G. Scott, "Assessment of cameras for low intensity acquisitions," Central Laser Facility: Annual Report No. 37, 2017/2018, <https://www.clf.stfc.ac.uk/Gallery/37%20-%20Dasgupta%20camera%20PDF.pdf>.
- ²¹S. Singh, C. D. Armstrong, N. Kang, L. Ren, H. Liu, N. Hua, D. R. Rusby, O. Klimo, R. Versaci, Y. Zhang *et al.*, "Bremsstrahlung emission and plasma characterization driven by moderately relativistic laser-plasma interactions," *Plasma Phys. Controlled Fusion* **63**, 035004 (2021).
- ²²T. S. Daykin, H. Sawada, Y. Sentoku, F. N. Beg, H. Chen, H. S. McLean, A. J. Link, P. K. Patel, and Y. Ping, "Characterization of fast electron divergence and energy spectrum from modeling of angularly resolved bremsstrahlung measurements," *Phys. Plasmas* **25**, 123103 (2018).
- ²³R. J. Gray, R. Wilson, M. King, S. D. R. Williamson, R. J. Dance, C. Armstrong, C. Brabetz, F. Wagner, B. Zielbauer, V. Bagnoud *et al.*, "Enhanced laser-energy coupling to dense plasmas driven by recirculating electron currents," *New J. Phys.* **20**, 033021 (2018).
- ²⁴W. R. Inc., Mathematica, Version 12.3.1, Champaign, IL, 2021.
- ²⁵F. Gao and L. Han, "Implementing the Nelder-Mead simplex algorithm with adaptive parameters," *Comput. Optim. Appl.* **51**, 259–277 (2012).
- ²⁶J. A. Nelder and R. Mead, "A simplex method for function minimization," *Comput. J.* **7**, 308–313 (1965).
- ²⁷C. J. Hooker, J. L. Collier, O. Chekhlov, R. Clarke, E. Divall, K. Ertel, B. Fell, P. Foster, S. Hancock, A. Langley *et al.*, "The Astra Gemini project—A dual-beam petawatt Ti:Sapphire laser system," *J. Phys. IV* **133**, 673–677 (2006).
- ²⁸A. S. Pirozhkov, Y. Fukuda, M. Nishiuchi, H. Kiriya, A. Sagisaka, K. Ogura, M. Mori, M. Kishimoto, H. Sakaki, N. P. Dover *et al.*, "Approaching the diffraction-limited, bandwidth-limited petawatt," *Opt. Express* **25**, 20486–20501 (2017).
- ²⁹H. Kiriya, A. S. Pirozhkov, M. Nishiuchi, Y. Fukuda, K. Ogura, A. Sagisaka, Y. Miyasaka, H. Sakaki, N. P. Dover, K. Kondo *et al.*, "Status and progress of the J-KAREN-P high intensity laser system at QST," *High Energy Density Phys.* **36**, 100771 (2020).
- ³⁰H. Kiriya, A. S. Pirozhkov, M. Nishiuchi, Y. Fukuda, A. Sagisaka, A. Kon, Y. Miyasaka, K. Ogura, N. P. Dover, K. Kondo *et al.*, "Petawatt femtosecond laser pulses from titanium-doped sapphire crystal," *Crystals* **10**, 783 (2020).
- ³¹The science and technology behind EPAC (2019), available at <https://www.clf.stfc.ac.uk/Pages/EPACs-Science.aspx>; accessed March 16, 2021.
- ³²A. Pirozhkov, A. Sagisaka, K. Ogura, T. Esirkepov, B. Gonzalez Izquierdo, A. Shatkhin, E. Vishnyakov, C. Armstrong, T. Pikuz, M. Alkhimova, S. Pikuz, W. Yan, T. Jeong, S. Singh, P. Hadjisolomou, O. Finke, G. Grittani, M. Nevrkla, C. Lazzarini, A. Velyhan, T. Hayakawa, Y. Fukuda, J. Koga, M. Ishino, K. Kondo, Y. Miyasaka, A. Kon, M. Nishikino, A. Kolesnikov, E. Ragozin, D. Khikhlikha, I. Tsygvintsev, V. Gasilov, D. Kumar, J. Nejdil, D. Margarone, P. Satorov, S. Weber, M. Kando, H. Kiriya, G. Korn, D. Neely, K. Kondo, S. Bulanov, and T. Kawachi, "Generation of hard x-rays at intensities approaching 1022 W/cm², presented at Nuclear Photonics, 9 June 2021, Japan, [S23-37 P] (2020).